

# Improving the robustness of 3D turbo spin echo imaging to involuntary motion

Guobin Li · Maxim Zaitsev · Martin Büchert ·  
Esther Raithel · Dominik Paul · Jan G. Korvink ·  
Jürgen Hennig

Received: 3 April 2014 / Revised: 14 October 2014 / Accepted: 28 October 2014 / Published online: 20 November 2014  
© ESMRMB 2014

## Abstract

**Objective** 3D TSE imaging is very prone to motion artifacts, especially from uncooperative patients, because of the long scan duration. The need to repeat this time-consuming 3D acquisition in the event of large motion artifacts substantially reduces patient comfort and increases the workload of the scanner.

**Materials and methods** A new sampling strategy enables homogenized collection of  $k$ -space data for 3D TSE imaging. It is combined with Frobenius norm-based motion-detection to enable freely stopped acquisition in 3D TSE imaging whenever excessive subject motion is detected.

**Results** The feasibility and reliability of the proposed method were demonstrated and evaluated in in-vivo experiments.

**Conclusion** It is shown that the additional overhead related to repeat scanning of the 3D TSE sequence as a result of patient motion can be substantially reduced by using the homogenized  $k$ -space sampling strategy with automatic scan completion as determined by Frobenius norm-based motion-detection.

**Keywords** 3D TSE · Subject motion · Motion artifacts · Compressed sensing

---

G. Li (✉) · M. Zaitsev · M. Büchert · J. Hennig  
Department of Radiology, Medical Physics, University Medical  
Center Freiburg, Breisacher Straße 60a, 79106 Freiburg,  
Germany  
e-mail: guobin.li@uniklinik-freiburg.de

E. Raithel · D. Paul  
Siemens Healthcare, Erlangen, Germany

J. G. Korvink  
Department of Microsystems Engineering — IMTEK,  
University of Freiburg, Freiburg, Germany

## Introduction

Compared with the conventional spin echo sequence, rapid acquisition with relaxation enhancement (RARE) [1], also called turbo spin echo (TSE) or fast spin echo (FSE), utilizes a series of refocusing pulses to acquire multiple echoes after a single excitation to accelerate imaging. Two-dimensional TSE has been a standard imaging sequence in clinical MR examinations for many years, and has been used in human imaging for a wide range of applications. In pursuit of high-resolution MR imaging, an advanced three-dimensional TSE variation, known as SPACE (sampling perfection with application optimized contrasts using different flip angle evolutions; Siemens); CUBE (GE); or VISTA (volume isotropic turbo spin echo acquisition; Philips) was proposed approximately a decade ago [2]. In this sequence a single slab is acquired with non-selective refocusing RF pulses, very long echo trains, and variable refocusing flip angles to alleviate the penalty of RF power deposition (SAR) and image blurring caused by T2-decay. Even with acceleration by parallel imaging, the acquisition time of a 3D TSE procedure can be approximately 6–8 min in dark-fluid T2-weighted head imaging and proton density-weighted knee imaging. Consequently, 3D TSE imaging with long scan durations is very prone to motion artifacts. In the typical clinic, image quality degradation as a result of motion artifacts is promptly assessed visually by the MR technician, and, if rated unacceptable, a repeat acquisition with the same procedure is typically attempted. Repeating lengthy examinations dramatically affects the workload on the scanner and the comfort of the patient.

Many techniques have been proposed to suppress or reduce motion artifacts in MR imaging [3]. Projection-like methods [4, 5] or PROPELLER [6] sacrifice some sampling efficiency to oversample the center of  $k$ -space

for the purpose of motion detection and correction. Similarly to PROPELLER, the SNAILS technique [7] enables in-plane motion correction of 2D acquisitions. Rigid-body motion during 3D acquisitions can be effectively corrected if accurate motion information is available in real-time during the acquisition, e.g. from an external tracking device [8–10]. If the host sequence contains a sufficiently long recovery period, orthogonal spiral (PROMO) or volumetric navigators can be used to detect and correct for motion [11, 12]. Prospective motion-correction methods are primarily effective in correcting for rigid motion, for example in head examinations, and can also require the setup of external motion tracking systems. Retrospective methods can be used for examinations with both rigid and non-rigid motion. These are well suited to correction for motion between individual scans of time-series examinations but of limited value for correction for motion within a single acquisition.

Motion may occur at any time during the scan. If spontaneous motion occurs at the beginning of a scan, data acquisition can be stopped and repeated without a significant time penalty. Currently this requires careful visual observation of the patient. The decision is based purely on the technician's experience. If a significant fraction of the scan has been completed, repetition carries an increasing time penalty. If motion occurs but remains unobserved, the whole scan may have to be repeated.

To alleviate the additional burden on the subjects and the workload on the scanner, we propose a new data-acquisition strategy in combination with compressed sensing (CS) reconstruction [13] to address the problem of spontaneous significant subject movements during structural 3D TSE imaging. Subject motion during data acquisition is monitored in real-time by navigators integrated into the imaging sequence. The scan is then stopped if significant motion is detected. Images are reconstructed on the basis of available acquired data by use of CS techniques. The new acquisition strategy is intended to increase the probability of obtaining acceptable image quality for clinical diagnosis, even in the absence of sophisticated motion-correction techniques or tracking devices.

A wide range of motion-tracking methods of different sophistication have been introduced for motion detection; these include use of FID/1D/2D/3D navigators, optical tracking systems, field probes, etc. [9, 14–22]. For simplicity, we chose dual-1D projections similar to those used by Lai et al. [19], and developed a reliable metric for quantification of the motion threshold.

In this paper we propose a dedicated data-acquisition strategy for achieving optimum image quality from interrupted 3D scans. A dual-1D projection scheme and a corresponding metric are proposed for detection of arbitrary motion during imaging without any advanced

motion-correction techniques. Both the data acquisition strategy and the motion-detection method are implemented in the 3D TSE sequence and evaluated by use of data acquired from healthy volunteers. Real-time feedback is used to process the navigator data and make decisions regarding whether to continue or finish scanning, depending on the motion detected.

## Materials and methods

### *K*-space sampling and view ordering

CS enables more flexible undersampling of *k*-space than conventional parallel imaging techniques in which *k*-space is usually required to be regularly undersampled to achieve a successful reconstruction (GRAPPA, SENSE etc. [23, 24]). In the proposed sampling strategy, *k*-space data were pseudo-randomly acquired in the Cartesian *ky*–*kz* plane with variable density Poisson-disc distribution. First, a sampling mask, which indicates the positions of the *k*-space data to be collected, was generated with the desired acceleration factor (referred to as the complete mask). Second, another sampling mask with the same variable density Poisson-disc distribution but with a greater acceleration factor was calculated (referred to as the basic mask). In the generation of the basic mask, all candidates were taken from the acquired views of the complete mask. A complementary mask was obtained by subtracting the basic mask from the complete mask. Therefore, the complete acquisition was composed of a basic acquisition and a complementary acquisition (Fig. 1). In actual image acquisition, data in the basic mask were acquired before acquisition of the data in the complementary mask. The data used for calibration of coil sensitivities in parallel imaging were collected during the basic acquisition.

Views were separately ordered within the basic acquisition and the complementary acquisition. To decouple the echo train length from the matrix size, a flexible view-ordering method was proposed for two types of reordering scheme in 3D TSE imaging: linear and radial [25]. Typically linear reordering is used in imaging with long TEs, and radial reordering is mainly used in imaging with short TEs. In this work, a consistent uniform distribution of the acquired views over the entire *k*-space at any phase of the data acquisition process is desired such that at any time during the acquisition uniform sampling coverage is achieved. Fully uniform sampling would require that randomly distributed points from the total *ky*–*kz* plane are selected within each echo train. This would lead to large distances between points sampled in successive echoes, which may lead to eddy current effects. Therefore the entire *ky*–*kz* plane is divided into *N* sections or sectors. The range covered within

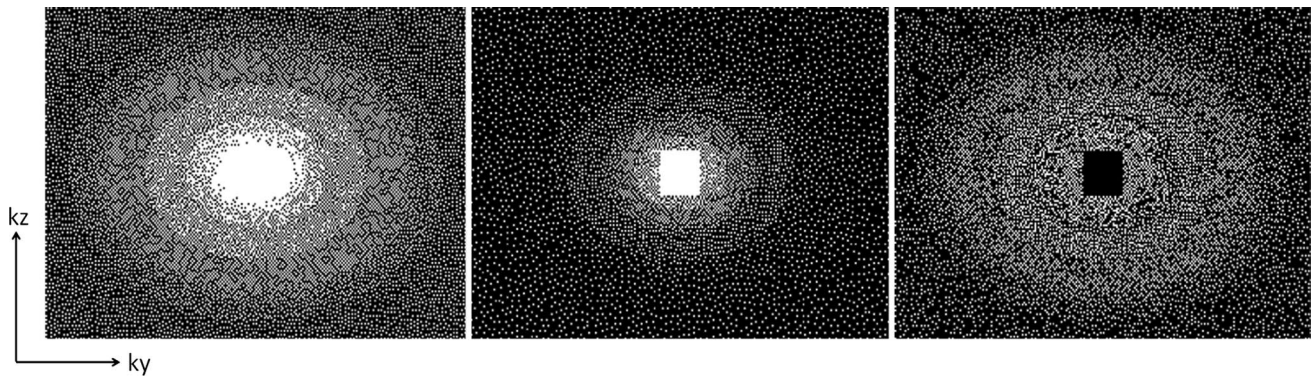
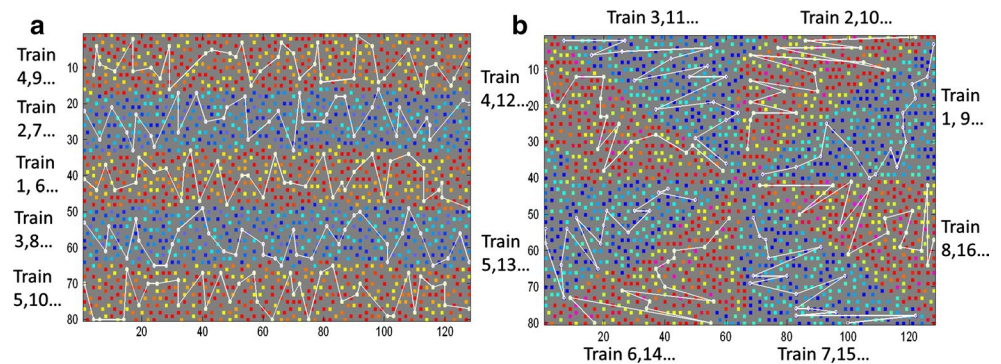


**Fig. 1** The  $k$ -space sampling mask in freely stopped 3D TSE imaging. The complete acquisition (*left*) is separated into basic acquisition (*middle*) and complementary acquisition (*right*)

**Fig. 2** Interleaving filling of  $k$ -space: linear reordering with 5 sections (**a**) and radial reordering with 8 sectors (**b**). Segmentation of the  $k$ -space is distinguished by colors. Train trajectories are randomized within each section or sector. Views with identical train numbers in each section or sector are indicated by the same color. One train trajectory in each section or sector is plotted



each echo train is limited to a section in linear reordering or a radial sector in radial reordering (Fig. 2). The trajectory of each echo train is randomized within each section or sector. Exact uniform sampling is therefore achieved by use of  $N$  echo trains, so  $N$  should not be very large; it should, on the other hand, be sufficiently large to avoid undesirably large jumps between successive echoes. In our examples we chose  $N$  to be between 5 and 16.

To achieve uniform sampling with limited randomization, flexible view ordering with interleaved filling of  $k$ -space was used. First, views were sequentially ordered by use of a method described elsewhere [25]. Second, for linear reordering, all trains were sorted on the basis of their distances to the  $k$ -space center and equally divided into  $N$  sections. Train numbers were reassigned by first randomly choosing  $N$  views with an identical echo number from the  $N$  sections (one view from each section). The first  $N$  train numbers were assigned to the  $N$  views in monotonic order according to their section number. Another set of  $N$  views was then chosen to assign the next  $N$  train numbers; this was repeated until all views have been included. For radial reordering, all trains were sorted on the basis of their coordinates in the  $k_\theta$  direction and divided into  $N$  sectors. Train

numbers were reassigned by use of the method used for adapted linear reordering. The same view-ordering method is applied, separately, to both the basic acquisition and complementary acquisition.

#### Motion detection

1D Navigator echoes were acquired at the end of each TR in 3D TSE imaging. As illustrated in Fig. 3, two thin slices perpendicular to the readout direction of the imaging acquisition were excited with a flip angle of  $8^\circ$ , and distances to the FOV center  $\pm 10$  mm. A gradient echo with only frequency encoding was acquired for each slice with a TE of 5 ms. The frequency encoding directions in the two slices were perpendicular to each other and also perpendicular to the readout direction of the imaging acquisition.

In the first few TRs (typically 2 TRs), the RF pulses in the navigator acquisition were switched off for two reasons:

1. to wait for the signal of the host sequence to reach shot-to-shot steady state; and
2. to collect data to calculate the statistics of the original noise level in navigator signals.



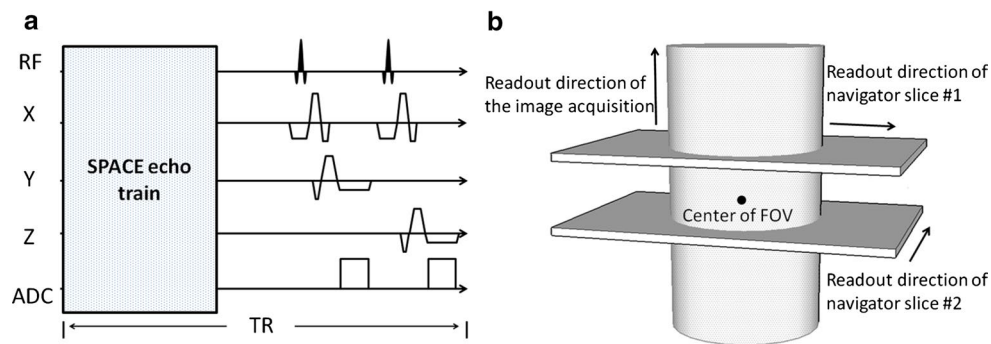


**Fig. 3** **a** The motion detection block inserted after the 3D TSE echo train at the end of each TR. Flow compensation gradients are applied in all directions to reduce interference from blood pulsation. **b** Dual

slice projection for motion detection. The readout directions in the two slices are perpendicular to each other, and also perpendicular to the readout direction of the image acquisition

The signal evolution in each TR is mainly dominated by the large flip angles in 3D TSE echo trains. On the basis of simulation results described in the next section, the effect of navigator acquisition on the steady state is negligible. The first navigator acquired with an RF pulse was used as reference for motion detection in subsequent TRs.

On the basis of the configuration above, a metric for detection of both rigid motion and non-rigid motion of the object occurring in any direction is proposed as follows.

All acquired navigator echoes are transformed into image space by performing an inverse Fourier transform. The reference profile of one of the navigator slices is described as:

$$A = \begin{bmatrix} a_{R11}, a_{I11} & \cdots & a_{R1n}, a_{I1n} \\ \vdots & \ddots & \vdots \\ a_{RK1}, a_{IK1} & \cdots & a_{RKn}, a_{IKn} \end{bmatrix}. \quad (1)$$

Here,  $n$  denotes the number of channels,  $K$  denotes the number of pixels selected from the profile, and  $R$  and  $I$  represent the real and imaginary values of the pixels.

A profile acquired and reconstructed in one of the following TRs is described as:

$$B = \begin{bmatrix} b_{R11}, b_{I11} & \cdots & b_{R1n}, b_{I1n} \\ \vdots & \ddots & \vdots \\ b_{RK1}, b_{IK1} & \cdots & b_{RKn}, b_{IKn} \end{bmatrix}. \quad (2)$$

Any element in **A** or **B** is composed of two parts: a constant signal and random noise with normal distribution. The noise component is independent and identically distributed in any element. Therefore, all elements in **A** and **B** are random variables with normal distribution; they have different mean values but identical variance  $\sigma^2$ , which is also the variance of the original noise and can be estimated from the noise scans in the beginning of the measurement.

Subtraction of **B** from **A** gives:

$$D = A - B$$

$$= \begin{bmatrix} a_{R11} - b_{R11}, a_{I11} - b_{I11} & \cdots & a_{R1n} - b_{R1n}, a_{I1n} - b_{I1n} \\ \vdots & \ddots & \vdots \\ a_{RK1} - b_{RK1}, a_{IK1} - b_{IK1} & \cdots & a_{RKn} - b_{RKn}, a_{IKn} - b_{IKn} \end{bmatrix}. \quad (3)$$

The Frobenius norm of the profile change **D** is defined as:

$$\|D\|_F = \sqrt{\sum_i^K \sum_j^n (a_{Rij} - b_{Rij})^2 + (a_{Iij} - b_{Iij})^2}. \quad (4)$$

The Frobenius norm is used below for direct quantification of the change in the profile caused by any type of object movement, including translation, rotation, and non-rigid deformation, or even by non-motional signal changes.

In the condition of no motion occurring between **A** and **B**, then the elements in **D** are also normally distributed with zero mean and variance  $2\sigma^2$ . It can be inferred that  $\|D\|_F$  is associated with a chi distribution [26], with probability density function:

$$P_{\|D\|_F}(x) = \frac{1}{\Gamma(nK)(\sqrt{2}\sigma)^2} \left( \frac{x}{2(\sqrt{2}\sigma)^2} \right)^{nK-1} \times x^{nK} \exp\left( \frac{-x^2}{2(\sqrt{2}\sigma)^2} \right). \quad (5)$$

Here,  $\Gamma(nK)$  is the gamma function.

The mean value of  $\|D\|_F$  is:

$$m_{\|D\|_F} = \frac{1 \cdot 3 \cdot 5 \cdot (2nK - 1)}{2^{nK-1}(nK - 1)!} \sqrt{\frac{\pi}{2}} \sqrt{2}\sigma, \quad (6)$$

and the standard deviation is:

$$s_{\|D\|_F} = \sqrt{2nK(\sqrt{2}\sigma)^2 - m_{\|D\|_F}^2}. \quad (7)$$

It is apparent the noise induced variation in  $\|D\|_F$  can be quantified on the basis of its statistics. But, because in our case  $nK$  is typically up to the order of a thousand, it becomes difficult to directly calculate the probability density function of the chi distribution. It has been observed that the chi distribution can be approximated by a normal distribution when  $nK$  is large enough [27, 28]:

$$\text{Chi}(x) \cong \text{Norm}\left(m_{\|D\|_F}, (s_{\|D\|_F})^2\right). \tag{8}$$

The threshold for motion detection could be:

$$TH = m_{\|D\|_F} + f * s_{\|D\|_F} \tag{9}$$

The probability of  $\|D\|_F$  exceeding the threshold of  $m_{\|D\|_F} + 4.0 * s_{\|D\|_F}$  is  $<0.01\%$  if noise is the only source of the profile variation. If any one of the measured  $\|D\|_F$  from the two navigator slices is greater than this threshold, one can conclude that motion occurred between the acquisition of profiles **A** and **B**, and technicians should be notified for a decision. However this threshold might be too sensitive to small movements, in which case the quality of the reconstructed image is only slightly degraded and interruption of the scan is not desired. A buffer for tolerating small motions must be added to the threshold to avoid unwanted interruption of the scan.

Because of the limited information obtained from the 1D projections, it is challenging to determine a universal analytical relationship between the measured profile change and the quantity of motion for displacements, rotations, and non-rigid deformations. However, it is a reasonable assumption for most in-vivo MR images that adjacent pixels are highly similar. Therefore squared differences between the pixels are expected to gradually increase when the corresponding distances increase, resulting in a monotonic relationship between the displacement of the object and the corresponding Frobenius norm of the profile change. This behavior, especially for small movements can be clearly observed in Fig. 4. On the basis of this assumption, a buffer corresponding to maximum tolerable motion can be approximately quantified on the basis of the following rationale: small movements of the object are generally modeled by the overall displacement of the acquired profile reference. Given the profile reference is shifted by  $t$  in units of pixels ( $0 \leq t \leq 1.0$ ) in the direction of the projection, the calculated buffer value for tolerating this kind of motion can be calculated on the basis of the gradient of the profile:

$$\text{buff} = (m_T + f * s_T) - (m_{\|D\|_F} + f * s_{\|D\|_F}), \tag{10}$$

in which

$$m_T = \frac{1 \cdot 3 \cdot 5 \cdot (2nK - 1)}{2^{nK-1} (nK - 1)!} \sqrt{\frac{\pi}{2}} \sqrt{2\sigma} {}_1F_1\left(-0.5, nK, \frac{-(tS)^2}{4\sigma^2}\right), \tag{11}$$

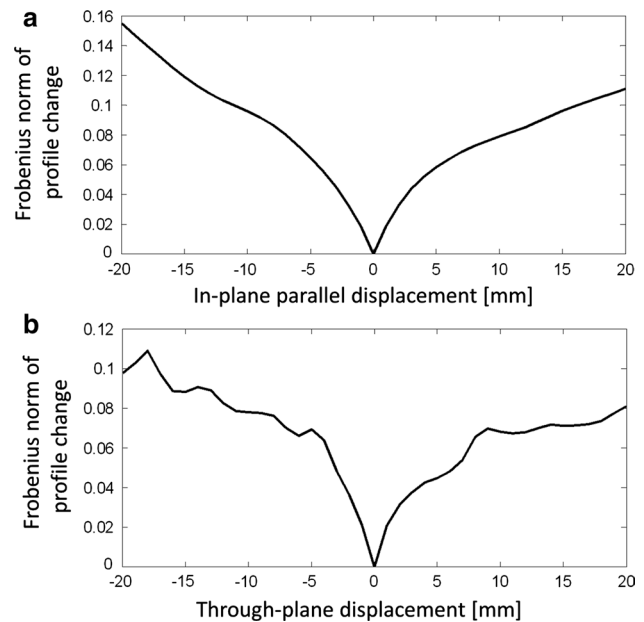


**Fig. 4** The monotonic relationship between the displacement of object and the Frobenius norm of the profile change. The shown curves are calculated based on a 3D head image. Navigator is obtained from the 1D projection of a slice. Displacement of the object is simulated by shifting the 3D image relative to the navigator. Note the similar monotonic relationship between the displacement of the object and the Frobenius norm of the profile change in cases of both in-plane displacement and through-plane displacement, especially when the absolute displacement is within 5 mm

and

$$s_T = \sqrt{2nK \left(\sqrt{2}\sigma\right)^2 + (tS)^2 - m_T^2}. \tag{12}$$

$$t = \frac{\Delta d}{\Delta x}. \tag{13}$$

where  $S$  is the signal component in the Frobenius norm of the profile gradient,  ${}_1F_1(a, b, z)$  is the confluent hypergeometric function,  $f$  is a scaling factor, set to a value  $>4.0$  in practice (typically 8.0 in our experiments) to tolerate the inaccuracy in the estimation of mean and standard deviation,  $\Delta x$  is the readout resolution of the navigator echoes, and  $\Delta d$  is the tolerable displacement of the object. The details of the derivation can be found in the “Appendix”.

The final threshold, which is used to judge whether motion is intolerable, is:

$$TH = (m_{\|D\|_F} + f * s_{\|D\|_F}) + \text{buff} = m_T + f * s_T. \tag{14}$$

It should be noted that, strictly speaking, the defined threshold value is only valid for in-plane motion. However, it may be approximately extended to through-plane motion under the assumption that the changes of the Frobenius

norm are isotropic for typical biological tissues and small displacements.

In each TR of the 3D TSE acquisition,  $\|D\|_F$  is updated, and compared with the threshold. If it is greater than the threshold, it can be assumed that intolerable motion occurred. For the two perpendicular projections, motion detection is separately performed. Motion is detected when any one of the two Frobenius norms exceeds its corresponding threshold. In all our experiments  $\Delta d$  was set to the read-out resolution of the image acquisition, which defined the threshold for motion detection.

Note that the final threshold above is predefined to tolerate small gross motion. In some imaged sections, blood pulsation in arteries induced additional profile changes in the navigators; this leads to underestimation of the navigator value and complicates determination of the actual threshold. Motion compensation gradients (Fig. 3) cannot completely suppress induced changes from blood pulsation. As a result, a simple preprocessing step was introduced to increase the robustness of the “gross” motion detection: in each calculated profile change, the pixel with the maximum intensity was located, and a fixed number of pixels around it (typically 20 % of the total pixels) were eliminated in the calculation of the Frobenius norm. This step further suppresses the interference from blood pulsation, but has minor effect on detection of gross motion.

### Image reconstruction

All image reconstruction with undersampling in the  $k$ -space was performed with  $l_1$ -SPIRiT [29, 30]. The solution  $x$  was obtained by iteratively minimizing the cost function below by using the nonlinear conjugate gradient method:

$$f = \|F_u x - y\|_2^2 + \lambda_1 \|\psi x\|_1 + \lambda_2 \|(G - I)(F x)\|_2^2 \quad (15)$$

where  $F_u$  is the Fourier transform operator with the applied  $k$ -space undersampling pattern corresponding to the finally used  $k$ -space data  $y$ ,  $\psi$  is the sparse transform (here, wavelet) of the individual coil images,  $I$  is an identity matrix,  $G$  is a series of convolution operators in SPIRiT for parallel imaging, and  $F$  is the Fourier transform operator. The third term enforces self-consistency of the acquired  $k$ -space data with the synthesized  $k$ -space data by exploiting the redundancy resulting from receipt of information from several channels.  $\lambda_1$  and  $\lambda_2$  are two scaling factors to adjust the trade-offs between data consistency, image sparseness, and parallel imaging. In all our experiments,  $\lambda_1$  was set to 0.005;  $\lambda_2$  was set to 0.3. Thirty-six iteration steps were used in each reconstruction.

The  $l_1$ -SPIRiT method was combined with POCS to reconstruct the datasets with explicit half-Fourier acquisition in linear reordering [31].

## Experiments

### Performance of sampling strategy

In the freely stopped 3D TSE, data acquisition might be stopped by technicians because of motion. In the incomplete acquisitions, fewer data are acquired, and the distribution of the acquired data in the  $k$ -space may deviate from the desired pattern. All these factors lead to a degraded quality of the reconstructed images. To evaluate the variation of the image quality in the interrupted 3D TSE imaging with different completion rates, the proposed sampling and view-ordering schemes have been implemented on two clinical MR scanners. A set of measurements was performed without intentional movements during the scanning. T2 weighted head imaging was performed on a 3.0T scanner (MAGNETOM Trio; Siemens, Erlangen, Germany) with a 12-channel receive coil and the settings: linear reordering;  $k$ -space matrix size  $256 \times 256 \times 176$  with 1.0 mm isotropic image resolution; echo train length = 252; scan duration = 4 min 08 s; acceleration factor of the complete acquisition = 2.5; basic acquisition = 35 % of the complete acquisition. Proton density weighted knee imaging was performed on a 1.5T scanner (MAGNETOM Espree; Siemens) with a 15-channel receive coil and the settings: radial reordering;  $k$ -space matrix size  $256 \times 246 \times 158$  with 0.6 mm isotropic image resolution; echo train length = 40; scan duration = 5 min 40 s; acceleration factor of the complete acquisition = 3.2; the basic acquisition amounts to 35 % of the complete acquisition. The same settings were also used for the healthy subject experiments. In the offline reconstruction, the acquired data were retrospectively removed on the basis of the view-ordering information to simulate the freely stopped scan. Different amounts of data were removed to simulate different completion. In the linear reordering scheme, two conventional acquisition strategies were simulated offline: sequential filling and centric filling. In the radial reordering scheme, the conventional sequential filling was simulated offline.

### Performance evaluation of motion detection with the Frobenius norm

Healthy subject experiments with voluntary movements (nodding, left–right rotation) were performed in head 3D TSE imaging. Navigators were acquired for tracking and detection of the motion, but scanning was not interrupted. At the same time, the motion of the object was accurately recorded by use of an MR-compatible optical tracking system (Metria Innovation, Milwaukee, USA), in which a planar tracking marker was mounted on the surface of the imaged body part, and a camera and related software were used to capture and calculate the pose of the marker

in six degrees of freedom [9]. The accuracy of the optical tracking system is up to 0.1 mm along the three axes, and  $0.07^\circ$  in all three rotations, so the motion trajectories recorded by the optical tracking system were taken as the ground truth to compare with the output of the Frobenius norm-based motion detection. The optical tracking system recorded the movements in real-time with temporal resolution of 12.5 ms. Optical tracking was selected as reference to quantify motion, because of its high accuracy, sampling rate, and its availability in our laboratory.

#### *Freely stopped scanning*

To evaluate the appropriateness of the threshold setting, 50 datasets from 11 healthy subjects were acquired. A different number of datasets was acquired in each session depending on the compliance of the subjects: 3 datasets (2 subjects), 4 datasets (2 subjects), 5 datasets (6 subjects), and 6 datasets (1 subject). Twenty datasets were from head imaging with rigid motion. Thirty datasets were from knee imaging with non-rigid motion. The proposed sampling strategy was applied. Navigators were acquired for tracking purposes only, and scanning was not interrupted. In all experiments, external healthy subjects were recruited, and were not provided with any instructions regarding movement during the scans. To further provoke subject movement because of discomfort, subjects were not positioned in a comfortable way with their consent in advance. An artificially prolonged acquisition procedure was set up. Each examination lasted about 1 h with continuous repetition of the proposed 3D TSE sequence. Subjects moved spontaneously at an unspecified time when they felt uncomfortable. Image reconstructions were performed in Matlab by use of two different methods: using all acquired data, and using only data acquired before the first detected motion. In the calculation of the threshold, the tolerable displacement of the imaged object was set to the readout resolution of the image acquisition. The reconstructed images were evaluated by two experienced research technicians unaware of the details of the experiment. Assessment was intentionally performed by technicians, because in a clinical environment, it is the technicians who decide on whether a scan is of sufficient quality to be passed on for diagnostic reading or must be repeated. The evaluation criteria were whether the signal-to-noise ratio (SNR) was sufficiently high and whether severe motion artifacts were present. Two technicians reached consent on whether or not they accepted the images for each reconstruction according to the criteria above.

The relative “average edge strength” (AES) was used to further quantify the suppression of motion artifacts in the simulated freely stopped scanning, which is defined as the AES of the interrupted acquisition divided by the AES of

the complete acquisition. The formula for calculating AES is described elsewhere [32]. The 10 outer-most slices at each side of the 3D volume were excluded from the calculation of AES to avoid interference from non-motion related artifacts.

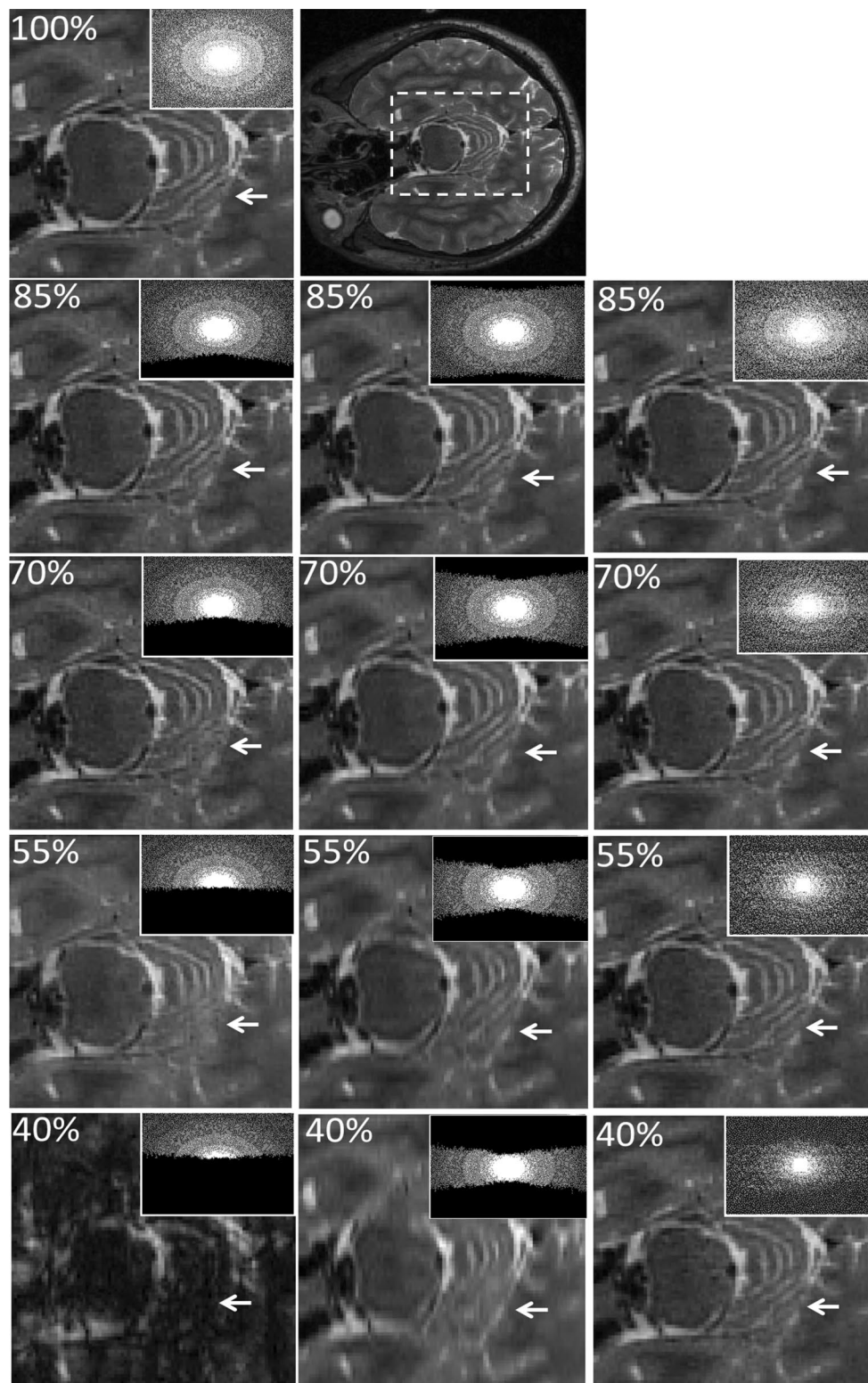
## Results

Figure 5 shows a magnified section of the reconstructed head images from the incomplete acquisitions with linear reordering. In conventional sequential filling of  $k$ -space, one section of  $k$ -space remained unfilled in the interrupted acquisitions. When completion was below 50 %, the unfilled region extended to the  $k$ -space center. Compared with sequential filling, the image quality of the incomplete acquisitions with centric filling of  $k$ -space was more stable when completion was reduced. However, the high-frequency data are missing along the  $kz$  direction which led to loss of resolution, especially for low completion. In the proposed interleaved filling of  $k$ -space, incomplete acquisitions resulted only in lower sampling density of the overall  $k$ -space. The magnified part of the reconstructed images shows that the image quality with the interleaved filling of  $k$ -space degraded more slowly when completion was reduced. In contrast, the image quality with the sequential filling of  $k$ -space degraded much more quickly on reduction of completion.

Figure 6 shows a magnified section of reconstructed knee images from incomplete acquisitions with radial reordering. It is again apparent that the reconstructed image quality in the proposed interleaved filling of  $k$ -space degraded more slowly and was always superior to that in the sequential filling of  $k$ -space when completion was reduced.

Figure 7 shows a comparison of the Frobenius norms of the profile changes with the actual measured motion given by the optical tracking system. The temporal resolution of the Frobenius norms of the profile changes depended on the repetition time of the MR scanning. The total translation and the total rotation of the marker were calculated. It was observed that the Frobenius norms of the profile changes oscillated slightly around a baseline when the object was kept still, but the values of the norms increased substantially when motion occurred. It successfully captured the movements of the object, but with much lower temporal resolution than that of the optical tracking system, which provides updates at 80 Hz. Results also show that two navigator slices with perpendicular frequency encoding directions had different sensitivities to specific motion.

Figure 8 shows a comparison of different threshold settings for motion detection. When the tolerable displacement was set to 3 times that of the readout resolution of



**Fig. 5** Reconstructed 3D head images from incomplete acquisitions with linear reordering. The full image of the selected slice is shown at the *top of the middle column* for orientation. Part of the image indicated by the *dashed box* is magnified for comparison of the three

acquisition strategies: sequential filling (*left column*), centric filling (*middle column*), and interleaved filling (*right column*). The corresponding sampling mask is given in the *upper right corners*



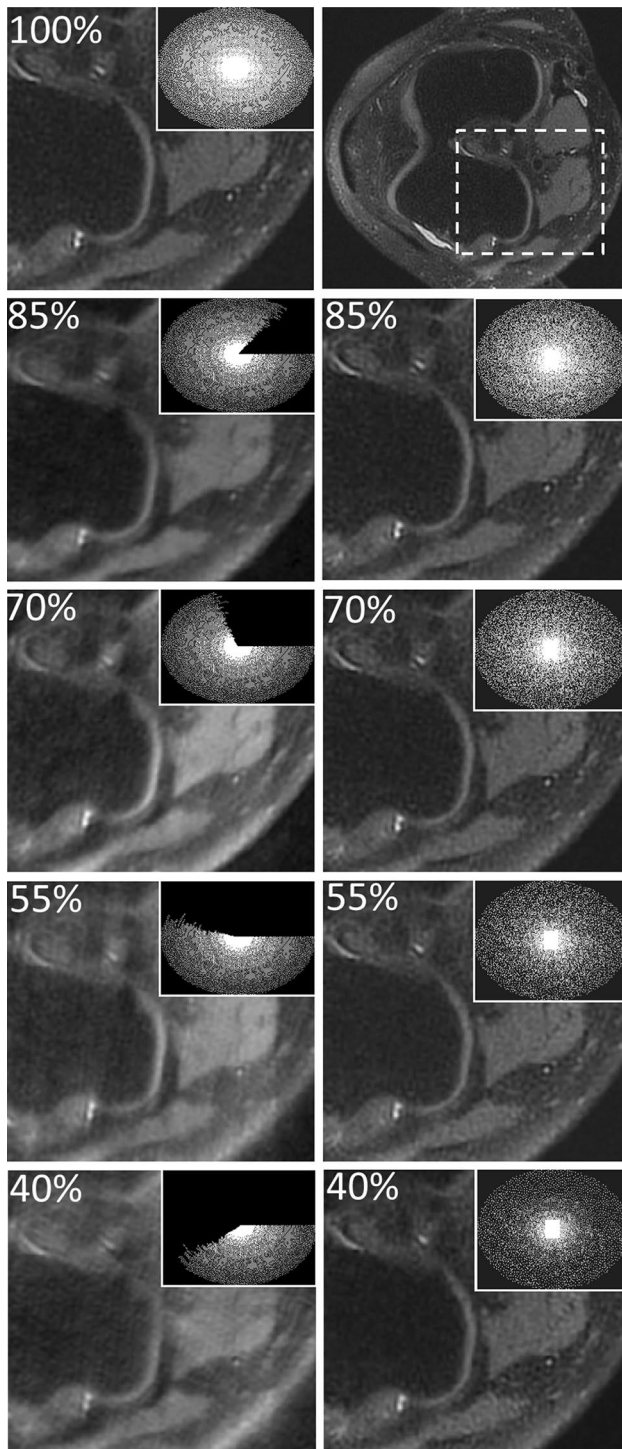


**Fig. 6** Reconstructed 3D knee images from incomplete acquisitions with radial reordering. The full image of the selected slice is shown at the *top of the right column*. Part of the image indicated by the *dashed box* is magnified for comparison of the two acquisition strategies: sequential filling (*left column*) and interleaved filling (*right column*). The corresponding sampling mask is given in the *upper right corners*

the image acquisition, visible motion artifacts, which might lead to incorrect diagnosis, can be observed in the reconstructed image. When the tolerable displacement was set to the readout resolution of the image acquisition, visible motion artifacts were substantially reduced.

Figure 9 shows a case in which significant motion in knee imaging was detected. By rejecting all the corrupted data, the motion-induced artifacts were substantially reduced compared with the reconstruction with all the acquired data (arrows in Fig. 9). Image quality was still acceptable, even though only 72 % of the data were acquired with the interleaved filling of  $k$ -space.

The 50 datasets were first reconstructed using all the acquired data without rejection of the motion-corrupted data. Blind evaluation of the images was performed. The results of the evaluation are given in Table 1. No motion was detected in 22 datasets, and all the reconstructed images were accepted. Among the datasets with detected motion, 22 out of 28 were not accepted. Figure 10 gives an overview of completion of the 28 datasets defined as the time of occurrence of the first significant motion. There were 6 datasets with detected motion but acceptable image quality. All were acquired with linear reordering, and corresponded to two cases.

1. In 2 datasets, navigators showed that the object moved at the very beginning of the acquisition. Approximately 1–2 echo trains were corrupted. Thereafter the subject stopped moving, and kept still during the rest of the acquisition.
2. In the other 4 datasets, navigators showed that the object remained static at the beginning, but movement occurred at the end of the acquisition. Only 2–3 echo trains were corrupted by the movement. The corrupted echo trains mainly filled the periphery of  $k$ -space.

For 17 of the 22 datasets with detected motion, basic acquisition was completed (completion >35 %). These datasets were then reconstructed without the corrupted data. The results from evaluation of the reconstructions are shown in Table 2. Twelve acquisitions were recovered by the freely stopped imaging strategy. Five acquisitions were still unacceptable because of insufficient SNR or loss of image details. An example of such an image is shown in Fig. 11. The free stop scanning image shows substantial reduction of the motion artifact, but the fine detail is still insufficient. This indicates that the amount of data to be scanned in the basic acquisition may vary for specific applications, depending on the number of receive channels and the sparsity in CS.

**Fig. 7** Comparison of the Frobenius norms of the profile changes (**a, b**) with the measured total rotation (**c**) and total translation (**d**) of the marker, which was mounted on the imaged body part in the optical tracking system. Motion leads to different changes in the Frobenius norms in the two navigators as indicated by 2 arbitrarily selected time points marked with vertical lines

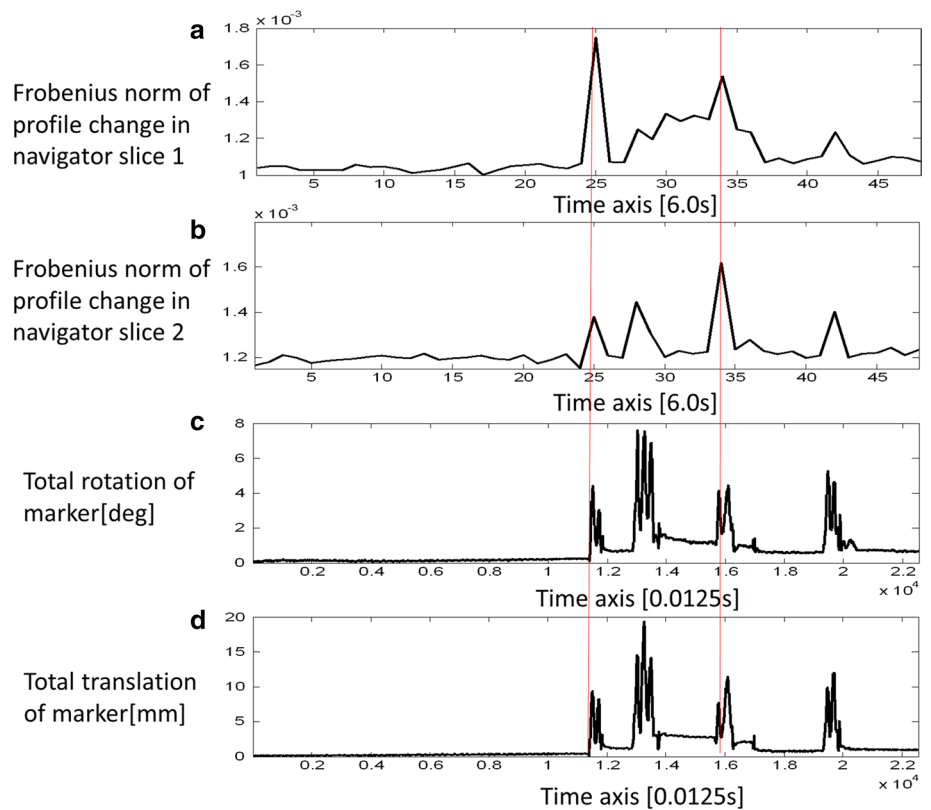
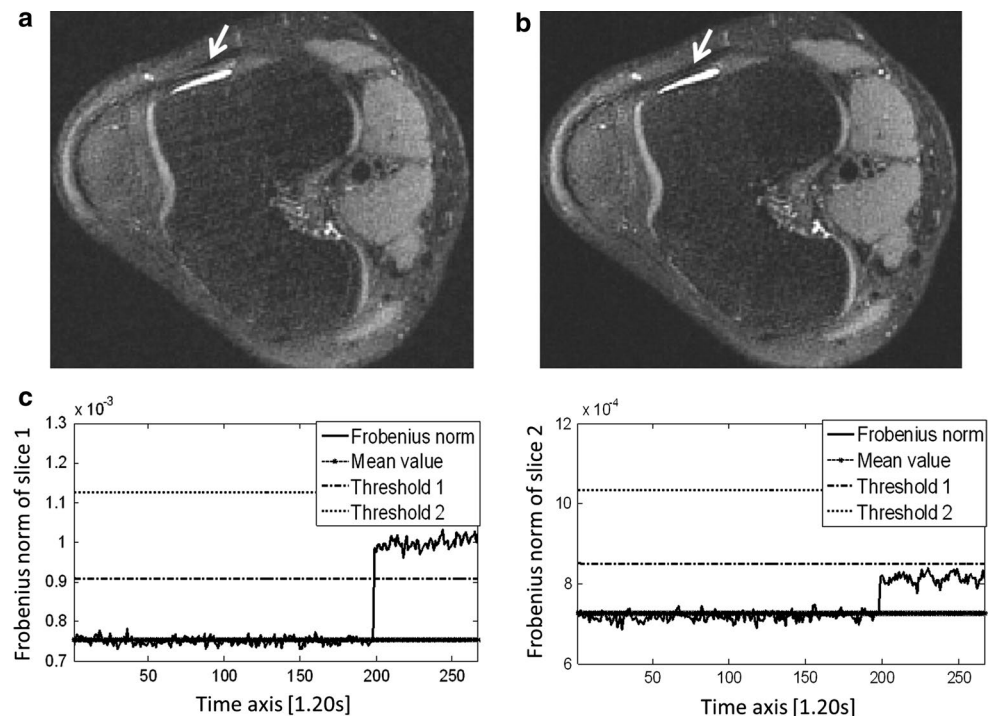


**Fig. 8** Comparison of two different threshold settings in knee imaging. The images were acquired with isotropic resolution 0.6 mm. In the calculation of Threshold 2 in (c), the tolerable displacement is set to 3 times of the readout resolution of image acquisition. No motion was detected, and all data were used to reconstruct the image (**a**). In the calculation of Threshold 1 in (c), the tolerable displacement is set to the readout resolution of image acquisition. Motion was detected at a late phase of the acquisition. 68 % of the acquired data were used to reconstruct the image (**b**). Motion artifacts (*arrows*), which might lead to incorrect diagnosis, can be observed in (**a**), but are substantially reduced in (**b**)



The relative average edge strength of the 17 interrupted acquisitions was calculated (Fig. 12). A clear improvement of the AES (Rel. AES >1) can be observed in the 12 interrupted acquisitions with accepted image quality (Fig. 12b).

In contrast with this, the improvement of the AES cannot be guaranteed in the interrupted acquisitions with unacceptable image quality. Two of the five datasets show a drop of the AES (Rel. AES <1) because of the loss of image

**Fig. 9** Comparison of normal 3D TSE imaging with freely stopped 3D TSE imaging when abrupt gross motion occurred at a late phase of the acquisition. **a** Image reconstructed with all acquired data; **b** image reconstruction with only the data acquired before the first detected motion; **c** calculated Frobenius norm of the profile change for the two slices

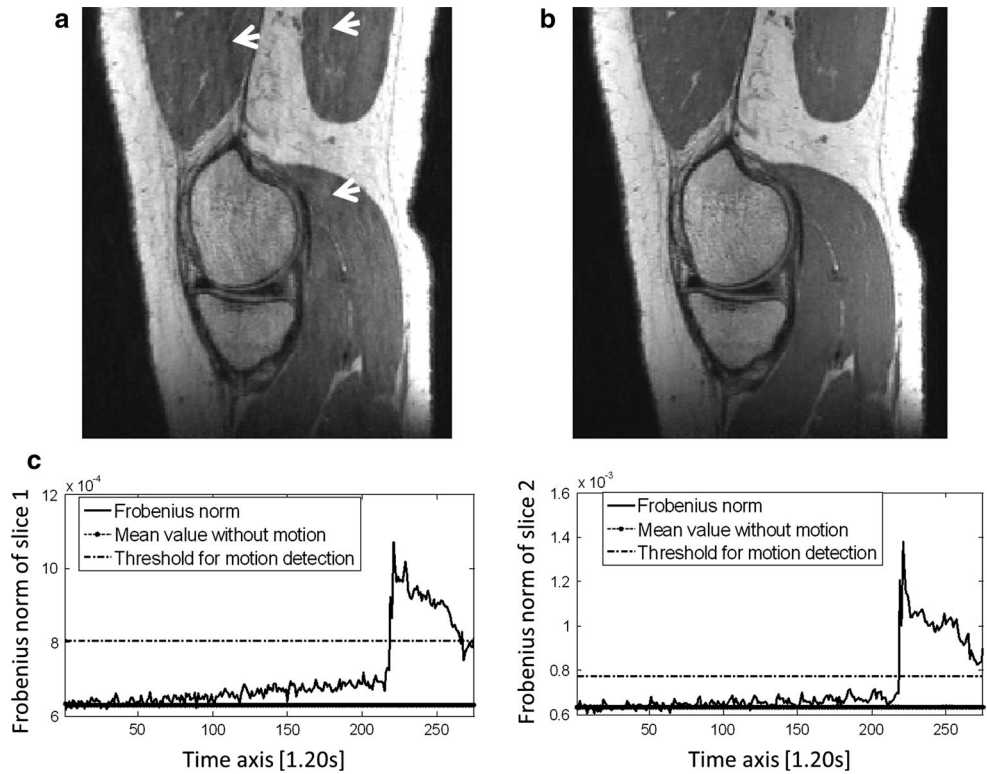


**Table 1** Evaluation of the reconstructions using all the acquired data in 3D TSE imaging

Motion detected	Image quality acceptable	Image quality unacceptable
28	6	22
No motion detected	Image quality acceptable	Image quality unacceptable
22	22	0

**Table 2** Evaluation of the reconstruction with only the data acquired before the first detected motion in freely stopped 3D TSE imaging

Reconstruction with freely stopped acquisition	Image quality acceptable	Image quality unacceptable
17 out of 22	12	5

Datasets represent cases with detected motion (completion rate >35 %), and unacceptable image quality in Table 1

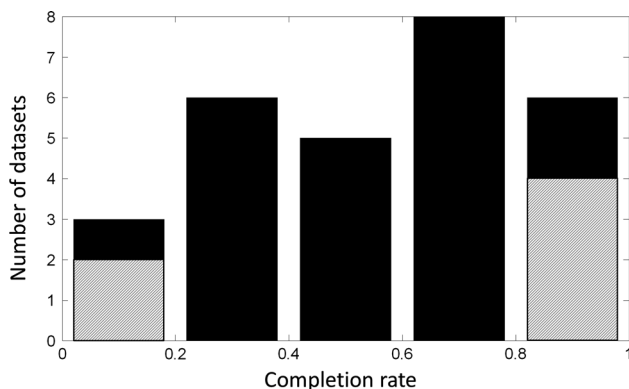


**Fig. 10** The statistics of completion at the time of occurrence of the first significant motion. Bars with diagonal shading represent the six datasets with detected motion, but accepted image quality

resolution caused by low completion (Fig. 12a). In the other three datasets, the increased AES indicates a reduction of motion artifacts in the interrupted acquisitions, but the residual artifacts are still too large to be accepted.

## Discussion

### Sampling strategy

In the interrupted acquisitions acquired with conventional sequential filling of  $k$ -space proposed in Ref. [25], the resulting empty regions in  $k$ -space lead to artifacts in reconstruction because of incomplete data. Especially in radial reordering or in linear reordering when completion is below 50 %, the interruption results in loss of important

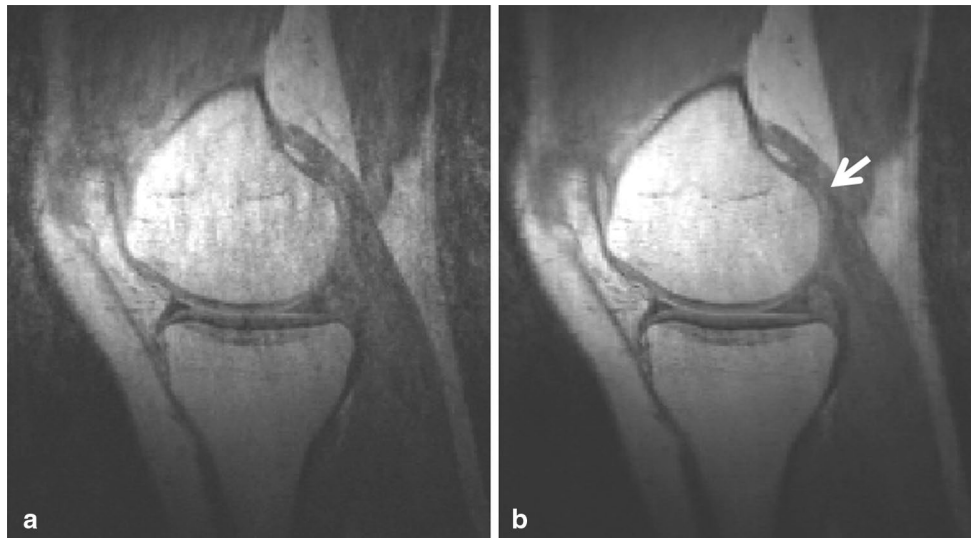


**Fig. 11** Example of an unaccepted image in the freely stopped scanning. The reconstructed image with corrupted data (**a**) shows severe motion artifacts. In the reconstructed image with the elimination of corrupted data (**b**), motion artifacts are substantially suppressed. However, (**b**) in this case is still not accepted because of loss of the

fine detail compared with the nominal 0.6 mm isotropic resolution, although 40 % of the data—more than the basic scan—have been acquired before the first detected motion. Note the poor delineation of the cartilage in (*arrow* in **b**)

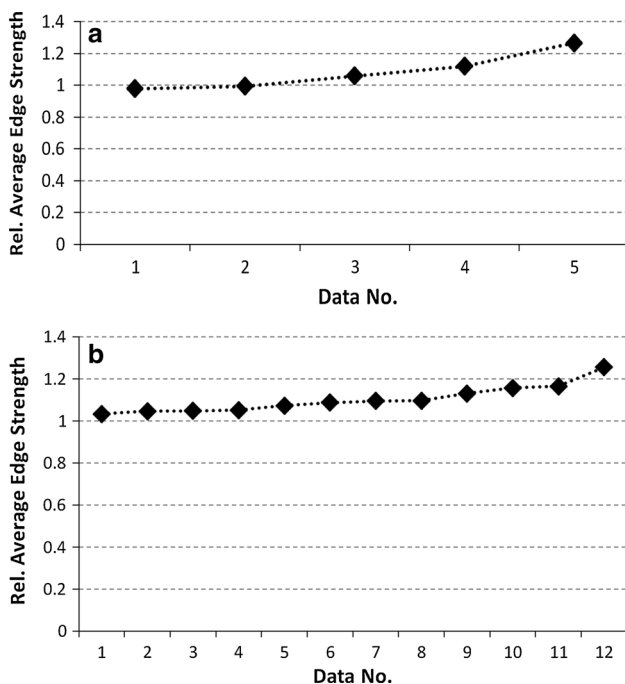


**Fig. 12** The relative average edge strength of the 5 interrupted acquisitions with unacceptable image quality (**a**), and the 12 interrupted acquisitions with acceptable image quality (**b**) in the experiments of simulated freely stopped scanning. Data are sorted in ascending order

data in the central region of  $k$ -space, which are used for calibration of coil sensitivities in parallel imaging. In our proposed sampling strategy for freely stopped scanning, the

desired full acquisition is composed of the basic acquisition and the complementary acquisition. The basic acquisition, containing the calibration data for parallel imaging is a minimum subset of the complete acquisition required to reconstruct clinically valuable images. If intolerable motion occurs during the basic acquisition, the scan can be aborted immediately, and reconstruction is not performed as the image quality is expected to be below that required for diagnosis. Once the basic acquisition is complete, the complementary acquisition is executed to improve the resolution and SNR of the resulting image. In the acquisition process, data will almost uniformly fill  $k$ -space using the proposed interleaved echo train trajectories with restricted randomization. More uniform filling can be obtained with fewer sections or sectors, but may lead to problems because of stronger fluctuation of the echo train trajectories, which may lead to more artifacts because of eddy currents. In our experiments,  $k$ -space was usually divided into 16 sections or sectors to balance the uniformity and the echo train fluctuation, even though for low values of  $N$ , no eddy current-induced artifacts were detected. More sections or sectors reduce the fluctuation of the echo trains, but the view ordering gradually turns to sequential filling.

Compared with the unified view ordering in conventional 3D TSE imaging, the  $k$ -space in our sampling strategy was divided into two parts with separate view orderings. Some echoes supposed to be filled in the  $k$ -space central region by the conventional acquisition were moved to high frequencies, mainly because the fully sampled calibration data in the  $k$ -space center were exclusively from



the basic acquisition. However, the resulting change in the  $k$ -space modulation can be neglected because the  $24 \times 24$  fully sampled calibration data used are relatively small compared with the full  $k$ -space size and only one or two echoes are affected in most 3D TSE imaging with whole volume coverage.

### Motion detection

Combination of dual-1D projection with the Frobenius norm of the profile change enables monitoring of motion in all dimensions. In-plane translation along any direction could be detected by at least one of the navigators as displacement of the acquired profile. Through-plane translation and rotation around any axis can be detected as the general deformation of the acquired profile. Because of the limitation of the maximum gradient amplitude and SNR, the thickness of the slice is much greater than its readout resolution. Therefore, the threshold calculated from the shifted profile reference might be overestimated for any motion in the through-plan direction. The proposed motion detection method is less sensitive to through-plane motion. In practice, the orientation of the navigators can be adjusted to cover the primary direction which is more prone to subject motion.

The Frobenius norm was chosen as the metric for motion detection because of several advantages compared to other methods:

1. it has a clear threshold which is obtained without any training procedure;
2. it is sensitive to any type of motion; and
3. no manual positioning of the navigators is required.

Profile-similarity or cross correlation metrics have been used to quantify the motion based on projections [33, 34]. However, these methods brought more mathematical challenges to distinguish the motion-induced change from the noise-induced change when SNR is poor. This can intuitively be understood by thinking of two cases:

1. noise is overwhelmingly greater than signal; and
2. signal is overwhelmingly greater than noise.

In case 1, the calculated profile-similarity or cross correlation randomly fluctuates in a wide range. It is nearly impossible to correctly identify the motion by directly comparing two acquired navigators without knowing the statistics of the noise. However, unlike the simple additive and subtractive operation in the Frobenius norm based method, multiplication and division are usually involved in calculation of similarity or correlation. If the combination of multiple receive channels is taken into account, there are nearly

no proved formulae for derivation of the noise distribution in such complicated cases in the literature. In case 2, noise-induced perturbation is well suppressed by the correlation calculation. Motion can be identified by directly comparing values from two navigators with a high probability of success. However, SNR depends on contrast, receive coils, main field strength, etc. High SNR cannot be guaranteed in diverse applications. A training procedure [35] could be introduced to set up an empirical threshold in each examination with a hypothesis that the object is kept still during the training procedure, which is not always the case in a real experiment.

Edge detection [16–18] is also popular, but has several drawbacks:

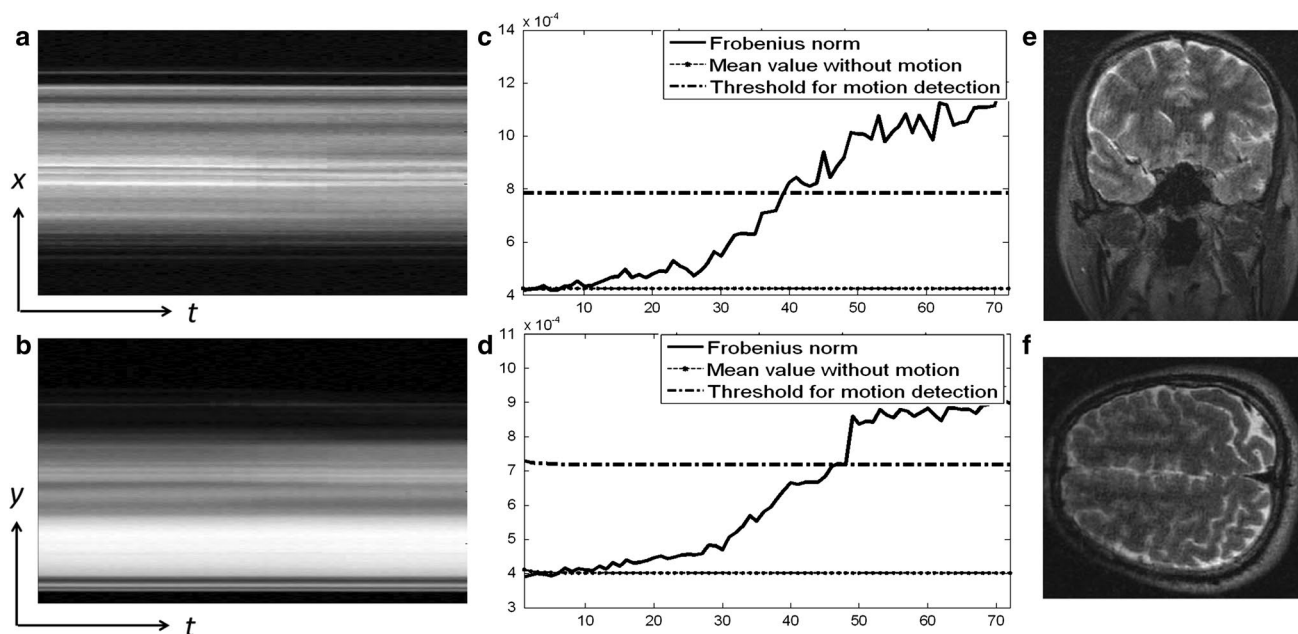
1. it is not sensitive to through-plane translations and rotations, especially when the object is almost spherical, for example, the rotation of the head around the head-foot axis;
2. high SNR is usually required for robust detection of edges, which cannot be guaranteed in practice when using surface receive coils with limited sensitivity.

Figure 13 shows a case of gradual motion, which is nearly undetectable by edge detection but successfully captured by the Frobenius norm of the profile change. Manually positioning of the navigators can improve the robustness of edge detection, like that used for detection of the diaphragmatic dome in body or cardiac examinations, but requires additional time for setup.

In typical 3D TSE imaging, the effective echo train duration is usually <30 % of the TR. Acquisition of the navigator echoes is inserted into the empty part of the TR, which does not prolong the total scan duration. In our experiments, the flip angle used to acquire the navigator echoes was  $8^\circ$ . Extended phase graph (EPG) algorithm-based simulations show that the attenuation of synovial fluid ( $T1/T2 = 3.6/0.7$  s) in typical knee imaging was <2 %, which is almost invisible in practice and can be neglected [36–38]. The effect of navigator acquisition on other tissues is even smaller, and is, therefore, not taken into account.

The Frobenius norm-based motion detection should be prudently applied in the imaged parts with interference from local motion, e.g. swallowing in C-spine imaging, which may cause false positive detection. This kind of occasional interference can be mitigated by confirming the gross motion with navigators from multiple TRs. Known sources of local and irrelevant motion can be ignored in calculation of the Frobenius norm.

The buffer for tolerating small motions was calculated in this work on the basis of the in-plane displacement. If the similarity between adjacent pixels does not reduce isotropically, the threshold may be overestimated



**Fig. 13** Capture of gradual motion by Frobenius norm of the profile change: **a, b**, profiles of two slices with perpendicular readout directions; **c, d**, calculated Frobenius norms of the corresponding profile differences and the threshold for motion detection; **e, f**, reconstructed

images with all acquired data. These results show that gradual motion is almost invisible in the measured profiles, but successfully detected by Frobenius norm. The severe motion artifacts in the reconstructed images reveal the validity of the detection

or underestimated for through-plane motion. However, in our simulations with 3D images representing different anatomic structures, we found that the Frobenius norm of the profile change varies quite isotropically along all directions, especially for small movements, as can be seen in Fig. 4.

#### Freely stopped scanning

The statistics of the 28 subject datasets with detected motion shows that the first motion occurred at any time in the scan (Fig. 10). This may not exactly reflect the behavior of the patients in clinical practice. However, the proposed method always improves the throughput of the 3D TSE imaging in the following ways:

1. Time is saved by detecting the motion early, and making the decision early. Technicians do not need to wait for the end of the acquisition to check the image quality.
2. If motion happens at a late phase of the acquisition, images with sufficient quality can still be obtained by using the proposed sampling strategy. No repetition was needed in most of these cases (12 out of 17 cases; Table 2). In a special case, similar to that observed in our experiments in which the subject moved at the very beginning of the acquisition (the 5th TR), but kept still during the rest of the time, motion detection leads to

unwanted interruption. However, the cost of the kind of interruption is almost negligible.

Further investigations are required to determine optimum values for the size of the basic scan and for reliable assessment of the motion threshold; both may depend on the body region and the medical condition under study. In this work, the freely stopped scanning was mainly demonstrated by 3D TSE imaging. However, this method can be directly applied in other 3D sequences with echo train acquisitions, e.g. 3D MPRAGE. By extending the concept of uniform filling of  $k$ -space during data acquisition from 3D to 2D, the method can be easily extended to 2D imaging.

#### Compatibility with other methods

The proposed method of freely stopped scanning is composed of two parts: a dedicated sampling strategy for interrupted acquisition and a motion-detection scheme. In this work, description and preliminary evaluation of the concept were primarily based on normal structural 3D TSE imaging without any advanced motion-correction techniques, so a dual-1D navigator scheme was proposed for the real-time motion detection.

The proposed method can be combined with more sophisticated motion-correction techniques, such that the

dual-1D navigator scheme is replaced by more advanced 3D navigators or even external optical tracking systems [9–11]. With prospective motion correction the overall robustness of the scan to motion is substantially improved, but there is still some threshold at which the prospective correction fails—i.e. because field homogeneity relative to the displaced scanning region changes. Using our approach ensures that at least in cases when such drastic motion occurs after completion of the basic scan, uncorrupted images can be reconstructed. Similarly, in the combination with retrospective motion-correction techniques, the proposed sampling strategy also provides additional chance to obtain acceptable image quality when artifacts are not sufficiently suppressed by retrospectively eliminating the seriously corrupted data.

$$\|G\|_F = \sqrt{\sum_j^n \left( (a_{R,1,j} - a_{RKj})^2 + (a_{I,1,j} - a_{IKj})^2 \right) + \sum_i^{K-1} \sum_j^n \left( (a_{R,i+1,j} - a_{Rij})^2 + (a_{I,i+1,j} - a_{Iij})^2 \right)} \quad (17)$$

## Conclusion

To increase the likelihood of obtaining images of diagnostic quality from 3D TSE imaging in the presence of spontaneous motion, a combination of a freely stopped sampling strategy and a dual-1D navigator scheme with a Frobenius norm metric is proposed. The cost of the repetition of the scan is reduced by early detection of the motion when the proposed sampling method fails to rescue the acquisition. The feasibility of these techniques has been proved by in-vivo experiments.

**Acknowledgments** The authors thank Bettina Wernli and Jutta Will for acquisition of data and evaluation of image quality. The authors thank Michael Herbst for helping to perform the experiments with the optical tracking system. The authors thank Benjamin Knowles for his help with the manuscript and journal referees for their thoughtful comments. This work was supported through research collaboration by Siemens Healthcare, Erlangen, Germany.

**Conflict of interest** The authors declare that they have no conflict of interest.

**Ethical standards** All volunteer studies in this work have been approved by the ethics committee in the university medical center and have therefore been performed in accordance with the ethical standards laid down in the 1964 Declaration of Helsinki and its later amendments. The manuscript does not contain clinical studies or patient data.

$$S = \sqrt{\sum_j^n \left( (s_{R,1,j} - s_{RKj})^2 + (s_{I,1,j} - s_{IKj})^2 \right) + \sum_i^{K-1} \sum_j^n \left( (s_{R,i+1,j} - s_{Rij})^2 + (s_{I,i+1,j} - s_{Iij})^2 \right)} \quad (23)$$

## Appendix

Detailed derivation of the buffer for small movements is described below. To simplify the estimation, small

movements in an arbitrary dimension are modeled by the overall displacement of the object along the readout direction of the navigators, and is manifested as a shift of the acquired reference navigator profile.

Given the tolerable shift is within one pixel of the profile, the distribution of the Frobenius norm of the profile change can be obtained by use of the following steps:

Reference profile  $A$  is circularly shifted by one pixel in the readout direction to obtain  $A'$ . Because the noise levels of the corresponding pixels in  $A$  and  $A'$  are still statistically independent of each other, the Frobenius norm of the profile gradient  $G$  is

$$\|G\|_F = \|A - A'\|_F \quad (16)$$

$\|G\|_F$  is associated with the chi distribution, with the probability density function:

$$P_{\|G\|_F}(x) = \frac{S}{(\sqrt{2}\sigma)^2} \left(\frac{x}{S}\right)^{nK} \exp\left(\frac{-(x^2 + S^2)}{2(\sqrt{2}\sigma)^2}\right) I_{nK-1}\left(\frac{xS}{(\sqrt{2}\sigma)^2}\right) \quad (18)$$

The mean value is:

$$m_{\|G\|_F} = \frac{1 \cdot 3 \cdot 5 \cdot (2nK - 1)}{2^{nK-1} (nK - 1)!} \sqrt{\frac{\pi}{2}} \sqrt{2}\sigma {}_1F_1\left(-0.5, nK, \frac{-S^2}{4\sigma^2}\right) \quad (19)$$

The standard deviation is:

$$s_{\|G\|_F} = \sqrt{2nK(\sqrt{2}\sigma)^2 + S^2 - m_{\|G\|_F}^2} \quad (20)$$

Here  $I_{nK-1}$  is the modified  $(nK - 1)$ th order Bessel function of the first kind,  ${}_1F_1(a, b, z)$  is the confluent hypergeometric function, and  $S$  is the intensity of signal components in  $\|G\|_F$ , which is explicitly defined as:

$$a_{R,l,j} = s_{R,l,j} + n_{R,l,j} \quad (21)$$

$$a_{I,l,j} = s_{I,l,j} + n_{I,l,j} \quad (22)$$

Here  $s_{R,l,j}$  and  $s_{I,l,j}$  are the signal components in  $a_{R,l,j}$  and  $a_{I,l,j}$  respectively.  $n_{R,l,j}$  and  $n_{I,l,j}$  are noise.

$S$  in the  $\|G\|_F$  is an unknown variable, but can be estimated as follows:

$$\frac{m_{\parallel G\parallel F}}{m_{\parallel D\parallel F}} = {}_1F_1\left(-0.5, nK, \frac{-S^2}{4\sigma^2}\right) \tag{24}$$

Because  $nK$  is of the order of a thousand,  $m_{\parallel G\parallel F} \gg s_{\parallel G\parallel F}$ , it is feasible to use the calculated  $\parallel G\parallel F$  to approximate its mean value  $m_{\parallel G\parallel F}$ . We obtain:

$$\frac{\parallel G\parallel F}{m_{\parallel G\parallel F}} = {}_1F_1\left(-0.5, nK, \frac{-S^2}{4\sigma^2}\right) \tag{25}$$

An approximation of  $S$  is obtained by solving the above equation. Given the displacement of object is  $t(0 \leq t \leq 1.0)$  pixels in the navigators, pixel values in the displaced profile could be expressed as a linear combination of the original profile and the profile shifted by 1.0 pixel:

$$x'_m = tx_{m+1} + (1 - t)x_m \tag{26}$$

$$x'_m - x_m = tx_{m+1} + (1 - t)x_m - x_m = t(x_{m+1} - x_m) \tag{27}$$

If the object is displaced by  $t$  pixels, an estimate of the intensity of the signal components in the Frobenius norm of the profile change is  $tS$ . Therefore, the mean value and the standard deviation of Frobenius norm of the profile change can be estimated as:

$$m_T = \frac{1 \cdot 3 \cdot 5 \cdot (2nK - 1)}{2^{nK-1}(nK - 1)!} \sqrt{\frac{\pi}{2}} \sqrt{2}\sigma_1 F_1\left(-0.5, nK, \frac{-(tS)^2}{4\sigma^2}\right) \tag{28}$$

$$s_T = \sqrt{2nK\left(\sqrt{2}\sigma\right)^2 + (tS)^2 - m_T^2} \tag{29}$$

Therefore, a new threshold, which tolerates tiny displacements, can be set as:

$$TH_T = m_T + f * s_T \tag{30}$$

The additional buffer for tolerating tiny movements in the detection of patients' voluntary motion can be obtained from:

$$\text{buff} = (m_T + f * s_T) - (m_{\parallel D\parallel F} + f * s_{\parallel D\parallel F}) \tag{31}$$

This deduction can be easily extended to cases for which the shift of the reference navigator profile is more than 1.0 pixel.

**References**

1. Hennig J, Nauerth A, Friedburg H (1986) RARE imaging: a fast imaging method for clinical MR. *Magn Reson Med* 3:823–833
2. Mugler JP, Bao S, Mulkern RV, Guttmann CRG, Robertson RL, Jolesz FA, Brookeman JR (2000) Optimized single-slab three-dimensional spin-echo MR imaging of the brain. *Radiology* 216:891–899
3. Zaitsev M, Dold C, Sakas G, Hennig J, Speck O (2006) Magnetic resonance imaging of freely moving objects: prospective

real-time motion correction using an external optical motion tracking system. *Neuroimage* 31(3):1038–1050

4. Bhat H, Ge L, NIELLES-Vallespin S, Zuehlsdorff S, Li D (2011) 3D radial sampling and 3D affine transform-based respiratory motion correction technique for free-breathing whole-heart coronary MRA with 100 % imaging efficiency. *Magn Reson Med* 65:1269–1277
5. Anderson AG, Velikina J, Block W, Wieben O, Samsonov A (2013) Adaptive retrospective correction of motion artifacts in cranial MRI with multicoil three-dimensional radial acquisitions. *Magn Reson Med* 69:1094–1103
6. Pipe JG (1999) Motion correction with PROPELLER MRI: application to head motion and free-breathing cardiac imaging. *Magn Reson Med* 42:963–969
7. Liu C, Bammer R, Kim D, Moseley ME (2004) Self-navigated interleaved spiral (SNAILS): application to high-resolution diffusion tensor imaging. *Magn Reson Med* 52:1388–1396
8. Maclaren J, Herbst M, Speck O, Zaitsev M (2013) Prospective motion correction in brain imaging: a review. *Magn Reson Med* 69(3):621–636
9. Maclaren J, Armstrong BSR, Barrows RT, Danishad KA, Ernst T, Foster CL, Gumus K, Herbst M, Kadashevich IY, Kusik TP, Li Q, Lovell-Smith C, Prieto T, Schulze P, Speck O, Stucht D, Zaitsev M (2012) Measurement and correction of microscopic head motion during magnetic resonance imaging of the brain. *PLoS One* 7(11):e48088
10. Herbst M, Maclaren J, Weigel M, Korvink J, Hennig J, Zaitsev M (2012) Prospective motion correction with continuous gradient updates in diffusion weighted imaging. *Magn Reson Med* 67:326–338
11. White N, Roddey C, Shankaranarayanan A, Han E, Rettmann D, Santos J, Kuperman J, Dale A (2010) PROMO: real-time prospective motion correction in MRI using image-based tracking. *Magn Reson Med* 63:91–105
12. Alhamud A, Tisdall MD, Hess AT, Hasan KM, Meintjes EM, van der Kouwe AJW (2012) Volumetric navigators for real-time motion correction in diffusion tensor imaging. *Magn Reson Med* 68:1097–1108
13. Lustig M, Donoho D, Pauly JM (2007) Sparse MRI: the application of compressed sensing for rapid MR imaging. *Magn Reson Med* 58:1182–1195
14. Kober T, Marques JP, Gruetter R, Krueger G (2011) Head motion detection using FID navigators. *Magn Reson Med* 66:135–143
15. Fu ZW, Wang Y, Grimm RC, Rossman PJ, Felmlee JP, Riederer SJ, Ehman RL (1995) Orbital navigator echoes for motion measurements in magnetic resonance imaging. *Magn Reson Med* 34:746–753
16. Liu YL, Riederer SJ, Rossman PJ, Grim RC, Debbins JP, Ehman RL (1993) A monitoring, feedback, and triggering system for reproducible breath-hold MR imaging. *Magn Reson Med* 30:507–511
17. Du YP, Saranathan M, Foo TKF (2004) An accurate, robust and computational efficient navigator algorithm for measuring diaphragm positions. *J Cardiovasc Magn Reson* 6(2):483–490
18. Iwadata Y, Kanda K, Yamazaki A, Kosugi S, Tsukamoto T (2008) Navigator echo analysis hybridizing magnitude and phase edge detection. In: Proceedings of the 16th scientific meeting, international society for magnetic resonance in medicine, Toronto, p 1468
19. Lai P, Larson AC, Bi X, Jerecic R, Li D (2008) A dual-projection respiratory self-gating technique for whole-heart coronary MRA. *J Magn Reson Imaging* 28:612–620
20. Morita S, Ueno E, Suzuki K, Machida H, Fujimura M, Kojima S, Hirata M, Ohnishi T, Imura C (2008) Navigator-triggered prospective acquisition correction (PACE) technique vs. conventional respiratory-triggered technique for free-breathing 3D



- MRCP: an initial prospective comparative study using healthy volunteers. *J Magn Reson Imaging* 28:673–677
21. van der Kouwe AJW, Benner T, Dale AM (2006) Real-time rigid body motion correction and shimming using cloverleaf navigators. *Magn Reson Med* 56:1019–1032
  22. Haerberlin M, Kasper L, Barmet C, Brunner D, Pruessmann K (2013) Field decoupling for real-time prospective motion correction using gradient tones and concurrent field monitoring. In: Proceedings of the 21st scientific meeting, international society for magnetic resonance in medicine, Salt Lake City, p 304
  23. Griswold MA, Jakob PM, Heidemann RM, Nittka M, Jellus V, Wang J, Kiefer B, Haase A (2002) Generalized autocalibrating partially parallel acquisitions (GRAPPA). *Magn Reson Med* 47:1202–1210
  24. Pruessmann KP, Weiger M, Scheidegger MB, Boesiger P (1999) SENSE: sensitivity encoding for fast MRI. *Magn Reson Med* 42:952–962
  25. Busse RF, Brau AC, Beatty PJ, Bayram E, Michelich CR, Kijowski R, Rowley HA (2008) Flexible and efficient view ordering for 3D sequences with periodic signal modulation. In: Proceedings of the 16th scientific meeting, international society for magnetic resonance in medicine, Toronto, p 837
  26. Dietrich O, Raya JG, Reeder SB, Ingrisch M, Reiser MF, Schoenberg SO (2008) Influence of multichannel combination, parallel imaging and other reconstruction techniques on MRI noise characteristics. *Magn Reson Imaging* 26(6):754–762
  27. Fisher RA (1922) On the interpretation of  $\chi^2$  from contingency tables, and the calculation of P. *J R Stat Soc* 85(1):87–94
  28. Canal L (2005) A normal approximation for the Chi square distribution. *Comput Stat Data Anal* 48(4):803–808
  29. Lustig M, Pauly JM (2010) SPIRiT: iterative self-consistent parallel imaging reconstruction from arbitrary  $k$ -space. *Magn Reson Med* 64:457–471
  30. Murphy M, Alley M, Demmel J, Keutzer K, Vasanawala S, Lustig M (2012) Fast l1-SPIRiT compressed sensing parallel imaging MRI: scalable parallel implementation and clinically feasible runtime. *IEEE Trans Med Imaging* 31(6):1250–1262
  31. Doneva M, Börnert P, Eggers H, Mertins A (2010) Partial Fourier compressed sensing. In: Proceedings of the 18th scientific meeting, international society for magnetic resonance in medicine, Stockholm, p 485
  32. Aksoy M, Forman C, Straka M, Çukur T, Hornegger J, Bammer R (2012) Hybrid prospective and retrospective head motion correction to mitigate cross-calibration errors. *Magn Reson Med* 67:1237–1251
  33. Luo J, Konofagou EE (2010) A fast normalized cross-correlation calculation method for motion estimation. *IEEE Trans Ultrason Ferroelectr Freq Control* 57(6):1347–1357
  34. Fan Z, Zuehlsdorff S, Liu X, Li D (2012) Prospective self-gating for swallowing motion: a feasibility study in carotid artery wall MRI using three-dimensional variable-flip-angle turbo spin-echo. *Magn Reson Med* 67:490–498
  35. Li G, Zaitsev M, Meyer E, Paul D, Hennig J (2013) Free-stop scanning for 3D TSE. In: Proceedings of the 21st scientific meeting, international society for magnetic resonance in medicine, Salt Lake City, p 2590
  36. Weigel M, Schwenk S, Kiselev VG, Scheffler K, Hennig J (2010) Extended phase graphs with anisotropic diffusion. *J Magn Reson* 205(2):276–285
  37. Hennig J, Weigel M, Scheffler K (2004) Calculation of flip angles for echo trains with predefined amplitudes with the extended phase graph (EPG)-algorithm: principles and applications to hyperecho and TRAPS sequences. *Magn Reson Med* 51:68–80
  38. Han E, Gold G, Stainsby J, Wright G, Beaulieu C, Brittain J (2003) In-vivo T1 and T2 measurements of musculoskeletal tissue at 3T and 1.5T. In: Proceedings of the 11st scientific meeting, international society for magnetic resonance in medicine, Toronto, p 0450